

Control of Periodically-Waked Wind Turbines

Aemilius A. W. van Vondelen, Atindriyo K. Pamososuryo, Sachin T. Navalkar, J.W. van Wingerden

Abstract—Periodic wakes are created on upstream wind turbines by pitching strategies such as the Helix approach to enhance wake mixing and thereby increase power production for wind turbines directly in their wake. Consequently, a cyclic load is generated on the actuating turbine’s blades, but also on the waked wind turbine. While the upstream load is the result of the pitching required for wake mixing, the downstream load originates from interaction with the periodic wake and only causes fatigue damage. This study proposes two novel individual pitch control schemes in which such a periodic load on the downstream turbine can be treated: by attenuation or amplification. The former method improves the fatigue life of the downstream turbine, whereas the latter enhances wake mixing further downstream by exploiting the already-present periodic content in the wake; both validated on a three-turbine wind farm in high-fidelity large-eddy simulations. Fatigue damage reductions of around 10% were found in the load mitigation case, while an additional power enhancement of 6% was generated on the third turbine when implementing the amplification strategy. Both objectives can easily be toggled depending on a wind farm operator’s demands and the desired loads/energy capture trade-off.

Index Terms—Wake mixing, Helix, large-eddy simulation, individual pitch control, downstream wind turbine, synchronization

I. INTRODUCTION

REDUCING the cost of wind energy motivates the establishment of wind farms that profit from shared infrastructure, installation, and maintenance costs. Typically, a minimum spacing of 4-5 rotor diameters is maintained, balancing the benefits of shared costs against reduced farm-level energy production as a result of the wake effect. This event—a phenomenon occurring when up- and downstream wind turbines align with the wind direction—causes reduced production due to lower wind speed and increased loading from wake impingement [1].

The wake effect can lead to substantial power loss, estimated at up to 20%, or an equivalent increase in loads depending on the wind farm layout [2]. Several solutions for the wake effect have been proposed in the past, such as the axial induction control method [3], which derates upstream turbines to leave more energy in the wake for downstream turbines. Studies, however, have shown that the production increase is negligible, making them more suitable for load balancing within wind farms rather than overall production optimization [4].

A more promising remedy is wake steering, which commands a yaw misalignment in the upstream wind turbine

to reposition its wake [5]. In this approach, a steady-state optimum is found, balancing the performance loss as a result of the misalignment with the performance gain obtained by alleviating turbines downstream of the wake. Since the wake is only repositioned, it might still affect other turbines further downstream.

A different approach is suggested by [6], where the wake is reduced by promoting wake mixing through dynamic variation of the induction, a method known as Dynamic Induction Control. One implementation of this method is done by pitching periodically, hence creating a periodic structure in the wake [7]. Significant power gains are found in a two-turbine case; however, significant load increases due to thrust force variations are also shown [8].

Frederik et al. [9] propose a similar periodic actuation method that, instead of varying the thrust force’s magnitude, rotates the direction around its nominal direction, significantly reducing the strong tower loads and varying power production, while achieving even better performance. The Helix approach, as it is colloquially called, has since garnered attention in literature, as extensive large-eddy simulations (LES) [10] and wind tunnel studies [11] have been performed, with multi-sine variations to the baseline Helix also proposed [12]; all with promising results in terms of power gains.

Up until recently, little attention was given to control of the turbine in the Helix wake downstream, while it poses interesting questions. First, the periodic loading as a result of the Helix actuation on the upstream turbine can similarly be found on the downstream turbine. Korb et al. [13] show that applying the Helix with a specific phase shift on the downstream turbine yields an additional power gain on the third turbine. They, however, do not propose a method for attaining this phase difference in control action. Van Vondelen et al. [14] suggest a phase synchronization method, which can track the phase of the Helix wake, while similarly applying a control action downstream. However, in this method, the quality of the phase estimate depends strongly on the quality of the linear model, which changes for each operating case. It may therefore be challenging to obtain exact phase estimates.

The above studies investigate the control of a downstream turbine from a power optimization perspective, while the periodic load could also be mitigated to improve fatigue life. This study proposes a controller that can achieve both while relieving the control engineer from deriving a linear model for each operating case. The contributions are hence three-fold:

- 1) Derivation of a novel control scheme for control of periodically-waked wind turbines which can achieve:
 - a) Load rejection through regulation;
 - b) Power enhancement through synchronization by reference tracking;

Aemilius A. W. van Vondelen, Atindriyo K. Pamososuryo, and J.W. van Wingerden are with the Delft Center for Systems and Control, Delft University of Technology, Mekelweg 2, 2628 CD Delft, the Netherlands (e-mail: {A.A.W.vanVondelen, A.K.Pamososuryo, J.W.vanWingerden}@tudelft.nl). Sachin T. Navalkar is with Siemens Gamesa Renewable Energy B.V. Prinses Beatrixlaan 800, 2595 BN Den Haag, the Netherlands (e-mail:Sachin.Navalkar@siemensgamesa.com).

2) Evaluation of 1) in a three-turbine large-eddy simulation.

The remainder of this paper is organized as follows. Section II introduces the conventional individual pitch control and the Helix, after which Section III presents the main contributions: the derivation of the novel control schemes. The controllers corresponding to these schemes are tuned based on an identified model in Section IV. Section V presents the simulation setup and test cases. The results of each control objective are treated in separate sections. Section VI presents the results obtained after evaluating the proposed control scheme in LES for the load mitigation objectives, while Section VII analyzed results for the synchronized wake mixing objective. Lastly, conclusions are drawn in Section VIII.

II. INDIVIDUAL PITCH CONTROL AND THE HELIX

In this section, a brief introduction is given to individual pitch control for load reduction and the Helix approach for wake mixing (i.e. power enhancement), which is essential background information for understanding the proposed methods. These approaches both leverage the so-called Multi-Blade Coordinate (MBC) transformation, which is used to map the pitch control system from the *rotating coordinate frame* to the *fixed coordinate frame*. This methodology is exploited in this work to derive a novel coordinate transformation, which is used to map the pitch control system instead from the rotating coordinate frame to the *Helix coordinate frame*. As such, a considerable simplification of the pitch control system is obtained allowing for the derivation of a novel feedback controller for 1) load regulation, and 2) phase synchronization for power enhancement, both, in this section.

A. Conventional Individual Pitch Control

Significant challenges arise when larger rotors are used for wind turbines, which originate primarily from the increasing asymmetric loads caused by the spatiotemporal variability of the wind. Turbulence, wind shear, and tower shadow are amongst several phenomena that contribute to asymmetric loading, which acts on blades as they traverse through this varying wind field at the rotational frequency (once-per-revolution/1P), and its higher harmonics (2P, 3P, etc.). On the fixed structure, this loading propagates from the rotating system as a steady-state load at 0P and periodic loading at 3P, 6P, and higher in the case of a three-bladed turbine, as considered in this study.

As these loadings shorten fatigue life, and structural reinforcements are costly, individual pitch control for load reduction was proposed as a solution [15]. This feedback controller exploits the MBC transformation, which maps the blade root out-of-plane moment signals M_i , $i = 1, 2, 3$, for a three-bladed wind turbine in the rotating blade coordinate frame to the fixed (nonrotating) coordinate frame, where they are collective, tilt, and yaw moments (M_{col} , M_{tilt} , and M_{yaw} , respectively), a process known as *demodulation* (e.g. [16]):

$$\begin{bmatrix} M_{col} \\ M_{tilt} \\ M_{yaw} \end{bmatrix} = \frac{2}{3} \underbrace{\begin{bmatrix} 1/2 & 1/2 & 1/2 \\ \cos(\psi_1) & \cos(\psi_2) & \cos(\psi_3) \\ \sin(\psi_1) & \sin(\psi_2) & \sin(\psi_3) \end{bmatrix}}_{T_{cm}(\psi(t)=\omega_r t)} \begin{bmatrix} M_1 \\ M_2 \\ M_3 \end{bmatrix}, \quad (1)$$

where ψ_i is the azimuthal position of the blades and ω_r is the rotor velocity. Note that ω_r is taken constant here and through the remainder of this paper for ease of implementation and analyses. Although this is valid for low wind speed variations, the final formulation of the derivations of the main contributions will all depend on the time-dependent azimuth and can therefore be used with time-varying rotor speeds.

In this fixed coordinate frame, the individual pitch commands β_i can now be computed as decoupled collective, tilt, and yaw pitch commands (β_{col} , β_{tilt} , and β_{yaw} , respectively), allowing simple single-input single-output (SISO) control loops instead of more complex multiple-input multiple-output (MIMO) control. The 1P blade loading is demodulated here to the DC gain, or 0P frequency, where it is a simple bias that can easily be driven towards zero using integrator control, simplifying the pitch coordinate system significantly. In case of load imbalance, i.e. $M_1 \neq M_2 \neq M_3$, the 1P load is also demodulated to the 2P frequency [17].

Ultimately, the determined tilt and yaw commands are then mapped back to the individual blade rotating coordinate frame into pitch commands using the reverse transformation to *remodulate* the signal back into the original coordinate frame:

$$\begin{bmatrix} \beta_1 \\ \beta_2 \\ \beta_3 \end{bmatrix} = \underbrace{\begin{bmatrix} 1 & \cos(\psi_1 + \psi_{off}) & \sin(\psi_1 + \psi_{off}) \\ 1 & \cos(\psi_2 + \psi_{off}) & \sin(\psi_2 + \psi_{off}) \\ 1 & \cos(\psi_3 + \psi_{off}) & \sin(\psi_3 + \psi_{off}) \end{bmatrix}}_{T_{cm}^{-1}(\psi(t)+\psi_{off})} \begin{bmatrix} \beta_{col} \\ \beta_{tilt} \\ \beta_{yaw} \end{bmatrix}, \quad (2)$$

where ψ_{off} is an azimuth offset accounting for unmodeled actuator delays and blade flexibility, which is required to fully decouple the tilt and yaw channels [18].

The principle of modulation-demodulation is well-studied for communication networks but also sees several implementations in wind turbine control, of which IPC is the most famous example. Other implementations include tower side-side damping control [19], and in this work, the same principle will be applied in Section III to the frequency of the periodic load of the Helix.

B. The Helix approach

The Helix approach is an open-loop control strategy for power enhancement utilizing the MBC transformation to excite the blades with periodic tilt and yaw signals. These signals are determined by setting an amplitude, and a frequency, where the latter parameter is governed by the dimensionless Strouhal number:

$$St = \frac{f_e D}{U_\infty}, \quad (3)$$

where f_e is the excitation frequency of the tilt and yaw commands, D is the rotor diameter, and U_∞ is the free stream wind velocity. Strouhal values are generally selected between 0.2 and 0.4 as recommended by previous work [6], [9]. This leads to the following tilt and yaw pitch commands for Helix wake mixing:

$$\begin{bmatrix} \beta_{tilt} \\ \beta_{yaw} \end{bmatrix} = \begin{bmatrix} A \sin(\omega_e t) \\ A \sin(\omega_e t \pm \pi/2) \end{bmatrix}, \quad (4)$$

where A is the amplitude, usually no larger than 6 degrees due to practical constraints such as pitch rate limitations, and $\omega_e = f_e 2\pi$. Note that the collective pitch β_{col} is omitted in (4) since it is controlled by the collective pitch controller.

Two Helix variants exist, where setting $+\pi/2$ in β_{yaw} yields a clockwise (CW) and $-\pi/2$ a counter-clockwise (CCW) rotating Helix. Although the control commands are given at the same frequency in the fixed frame, the effective actuation frequency of the pitch actuation between CW and CCW variants in the rotating frame is different:

$$\beta_i = \beta_{col} + \cos(\psi_i)\beta_{tilt} + \sin(\psi_i)\beta_{yaw}, \quad (5)$$

which yields that the Helix frequency in the rotating frame is at the rotation frequency ω_r plus or minus the excitation frequency ω_e (or $1P \pm f_e$), depending on CW or CCW:

$$\begin{aligned} \beta_i &= \beta_{col} + A \cos(\omega_r t + \psi_i^0) \beta_{tilt} + A \sin(\omega_r t + \psi_i^0) \beta_{yaw}, \\ &= A \cos(\omega_r t + \psi_i^0) \sin(\omega_e t) \\ &\quad + A \sin(\omega_r t + \psi_i^0) \sin(\omega_e t \pm \pi/2) \\ &= A \sin[(\omega_r \pm \omega_e)t + \psi_i^0], \end{aligned} \quad (6)$$

where ψ_i^0 is the phase shift originating from the azimuthal position of blade $i = 1, 2, 3$ at time $t = 0$. Generally, the CCW Helix results in higher farm-level energy gains [9], [10], while the CW Helix is favored for lower damage to the pitch bearing [20], which can be explained by the lower effective actuation frequency of $1P - f_e$.

A consequence of employing the Helix approach is the generation of periodic loading, which impacts the fatigue life of the actuating turbine [20]. This loading, however, is also found on the downstream turbine, as reported by [8]. As such, it negatively impacts the fatigue life of the downstream turbine as well, but could potentially be attenuated using a downstream Helix load regulator. A different solution to this periodic loading would be to exploit the gain at this frequency to enforce wake mixing further downstream by amplifying the load slightly while preserving its phase. Both these ideas are developed in the next section.

III. NOVEL DOWNSTREAM CONTROLLERS

This section presents the main contributions of this work, the derivation of a downstream Helix load regulator, and a phase synchronization control scheme.

A. Downstream Helix load regulator

Now, the derivation of the novel downstream Helix load regulator is performed. The principle of modulation-demodulation is applied to transform the rotating coordinate frame of the pitch control system to the Helix coordinate frame, which demodulates the to-be-attenuated $1P + f_e$ load¹ to the DC gain. This diverges from the conventional MBC transformation which maps to the fixed coordinate frame ($1P$ frequency to DC gain). In the Helix coordinate frame, the Helix load can be regulated using two simple integrator control loops. An

¹In the remainder of this paper, the CCW Helix load of $1P + f_e$ is assumed, but note that this value can be substituted for CW Helix or any desired frequency that acts on the turbine rotor.

TABLE I: Demodulated loads in each reference frame.

| Load | Coordinate frame | | |
|------------------------------|------------------|-------|-------|
| | Rotating | Fixed | Helix |
| Wind-induced rotor asymmetry | $1P$ | DC | f_e |
| Helix | $1P \pm f_e$ | f_e | DC |

overview of the loads and their demodulated frequencies in different coordinate frames is given in Table I.

Let the MBC transformation (1) now include the excitation frequency ω_e to map to the Helix coordinate frame, we have:

$$\begin{bmatrix} M_{col,e} \\ M_{tilt,e} \\ M_{yaw,e} \end{bmatrix} = T_{cm}(\omega_t t) \begin{bmatrix} M_1 \\ M_2 \\ M_3 \end{bmatrix}, \quad (7)$$

where,

$$T_{cm}(\omega_t t) = \frac{2}{3} \begin{bmatrix} 1/2 & 1/2 & 1/2 \\ \cos(\psi_1 + \omega_e t) & \cos(\psi_2 + \omega_e t) & \cos(\psi_3 + \omega_e t) \\ \sin(\psi_1 + \omega_e t) & \sin(\psi_2 + \omega_e t) & \sin(\psi_3 + \omega_e t) \end{bmatrix},$$

where $M_{col,e}$, $M_{tilt,e}$, $M_{yaw,e}$ are the orthogonal moment axes in the Helix coordinate frame and $\omega_t = \omega_r + \omega_e$.

For ease of implementation, it is useful to decompose $T_{cm}(\omega_t t)$; thus, the angle sum identity is used:

$$\begin{bmatrix} \cos(\omega_r t + \omega_e t) \\ \sin(\omega_r t + \omega_e t) \end{bmatrix} = \begin{bmatrix} \cos(\omega_e t) & -\sin(\omega_e t) \\ \sin(\omega_e t) & \cos(\omega_e t) \end{bmatrix} \begin{bmatrix} \cos(\omega_r t) \\ \sin(\omega_r t) \end{bmatrix} \quad (8)$$

This allows the decomposition of (7) into:

$$\begin{bmatrix} M_{col,e} \\ M_{tilt,e} \\ M_{yaw,e} \end{bmatrix} = \underbrace{\begin{bmatrix} 1 & 0 & 0 \\ 0 & \cos(\omega_e t) & -\sin(\omega_e t) \\ 0 & \sin(\omega_e t) & \cos(\omega_e t) \end{bmatrix}}_{R(\omega_e t)} \times \underbrace{\frac{2}{3} \begin{bmatrix} 1/2 & 1/2 & 1/2 \\ \cos(\psi_1) & \cos(\psi_2) & \cos(\psi_3) \\ \sin(\psi_1) & \sin(\psi_2) & \sin(\psi_3) \end{bmatrix}}_{T_{cm}(\psi(t))} \begin{bmatrix} M_1 \\ M_2 \\ M_3 \end{bmatrix}, \quad (9)$$

with $R(\omega_e t)$ as a rotation matrix. Following a similar methodology, the reverse transformation is found as follows:

$$\begin{bmatrix} \beta_1 \\ \beta_2 \\ \beta_3 \end{bmatrix} = \underbrace{\begin{bmatrix} 1 & \cos(\psi_1) & \sin(\psi_1) \\ 1 & \cos(\psi_2) & \sin(\psi_2) \\ 1 & \cos(\psi_3) & \sin(\psi_3) \end{bmatrix}}_{T_{cm}^{-1}(\psi(t))} \times \underbrace{\begin{bmatrix} 1 & 0 & 0 \\ 0 & \cos(\omega_e t) & \sin(\omega_e t) \\ 0 & -\sin(\omega_e t) & \cos(\omega_e t) \end{bmatrix}}_{R^{-1}(\omega_e t)} \begin{bmatrix} \beta_{col,e} \\ \beta_{tilt,e} \\ \beta_{yaw,e} \end{bmatrix}. \quad (10)$$

The above derivation shows that mapping to the Helix coordinate frame is in fact a time-varying rotation applied to the system in the fixed coordinate frame. A schematic overview of the proposed control scheme in the Helix coordinate frame is shown in Fig. 1. Here, $M_{tilt,e}$ and $M_{yaw,e}$ are regulated using two SISO loops, which are schematically depicted in Fig. 2. Section IV will elaborate on the synthesis of these SISO controllers.

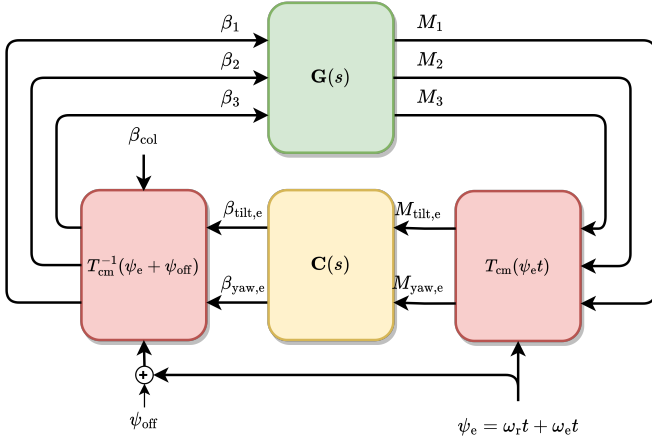


Fig. 1: Proposed control scheme in closed-loop.

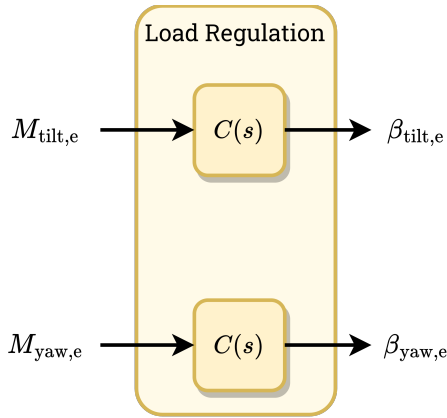


Fig. 2: Controller architecture 1: load regulation scheme.

The next section will show that, instead of attenuating the load caused by the actuating upstream turbine as derived above, the downstream turbine could also amplify this load, potentially leveraging the periodic content wake to extend the wake mixing further downstream.

B. Downstream Helix phase synchronization

The control architecture of the Downstream Helix load regulator may be extended to obtain a reference tracking controller, which can achieve phase synchronization with the load generated by the incoming wake. This is achieved by setting a reference to the $M_{\text{tilt},e}$ and $M_{\text{yaw},e}$ signals. Since the objective is phase synchronization, the phase should be preserved. Therefore it is first extracted from the measured signals as follows:

$$\phi_e = \text{atan2}(M_{\text{tilt},e}, M_{\text{yaw},e}). \quad (11)$$

Subsequently, an amplitude reference M_e^{ref} is defined, which, for amplification, and thus the propagation of the wake mixing strategy, should be set larger than the amplitude of the measured signals:

$$M_e^{\text{ref}} > M_e = \left\| \begin{bmatrix} M_{\text{tilt},e} \\ M_{\text{yaw},e} \end{bmatrix} \right\|_2. \quad (12)$$

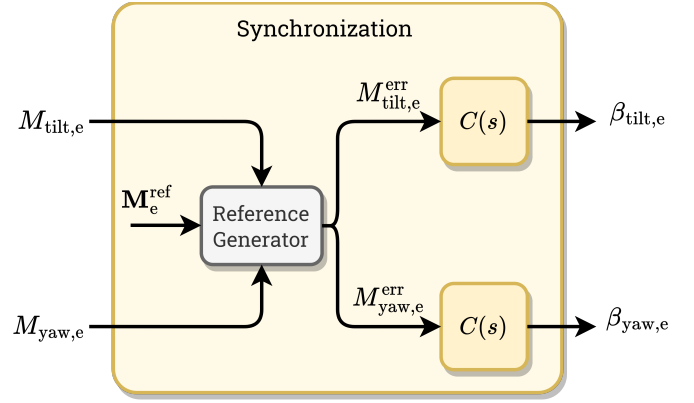


Fig. 3: Controller architecture 2: Helix synchronization scheme.

The error is then obtained as follows:

$$M_e^{\text{err}} = M_e - M_e^{\text{ref}} \quad (13)$$

Finally, the error signals are constructed as:

$$\begin{bmatrix} M_{\text{tilt},e}^{\text{err}} \\ M_{\text{yaw},e}^{\text{err}} \end{bmatrix} = M_e^{\text{err}} \begin{bmatrix} \sin(\phi_e) \\ \cos(\phi_e) \end{bmatrix}, \quad (14)$$

which preserves the phase of the periodic load. The control architecture of the phase synchronization method is schematically displayed in Fig. 3.

IV. CONTROLLER SYNTHESIS

After deriving the novel coordinate transformation in the previous section, this section aims to synthesize suitable proportional-integral-derivative (PID)-type controllers for the system in this framework through loop shaping. First, a linear model of the system (described in Section V) in Helix coordinates is identified by means of black box system identification. Then, using the identified model, PID-type controllers are tuned by using classical loop shaping techniques.

To identify a model, the optimized predictor-based subspace identification (PBSID_{opt}) [21] is used—an algorithm based on the well-known stochastic subspace identification method. This approach uses input/output data to estimate a linear model, which is obtained by persistently exciting the system with an input signal containing a broad spectrum of frequencies. As an excitation signal, pseudo-random binary noise is chosen, which is bandpass-filtered between 1e-3 and 1e2 rad/s to accommodate the actuator bandwidth. Since a linear identification method is used, the obtained model is linear-time invariant, and therefore only valid for a specific operating range.

The singular values yielded by the PBSID_{opt} method assist in determining an optimal identification order, where an order of 10 was found to correspond best to the spectral average of the input-output data as can be observed in Fig. 4. Note the difference in steady-state magnitude between the diagonal and off-diagonal transfers, denoting the degree of coupling the system has. A low coupling is desired, which simplifies controller synthesis as a SISO control loop can be used on each diagonal transfer. In this work, an azimuth offset of $\psi_{\text{off}} = 8$

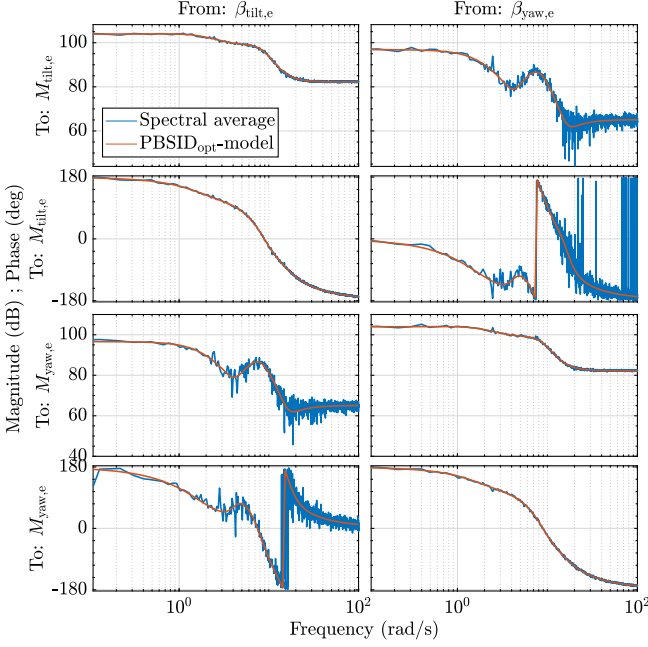


Fig. 4: Comparison of the PBSID_{opt}-identified model against the spectral averaged input/output data.

degrees is used to facilitate further decoupling [18]. However, the identified model is based on standalone OpenFAST, while further decoupling may be required if coupled to LES [22]. Further optimization of the optimal azimuth offset, however, is out of the current scope.

To control the loads at the ω_t frequency, the following diagonal SISO control structure is designed, as shown in Fig. 2 and 3:

$$\begin{bmatrix} \beta_{\text{tilt},e}(s) \\ \beta_{\text{yaw},e}(s) \end{bmatrix} = \underbrace{\begin{bmatrix} C(s) & 0 \\ 0 & C(s) \end{bmatrix}}_{\mathbf{C}(s)} \begin{bmatrix} M_{\text{tilt},e}(s) \\ M_{\text{yaw},e}(s) \end{bmatrix}, \quad (15)$$

where $\mathbf{C}(s)$ is shown in Fig. 2.

The tuning of PID controllers is done by frequency-domain loop shaping the transfer of the identified model and controller to achieve a certain crossover frequency ω_c :

$$L(s) = G(s)C(s), \quad (16)$$

where $L(s)$ is the loop transfer and $G(s)$ is the plant of the system in the Helix coordinate frame. A crossover frequency of $\omega_c = 0.115$ rad/s provided a good trade-off between transient response and sensitivity to noise for the initial controller design. Further adjustments in other controller concepts either increased or decreased this value. Two different types of controllers are implemented in (15); an integrator controller and a proportional-integral with low-pass filter (PI-LPF) controller:

$$C_I(s) = \frac{K_I}{s}, \quad (17)$$

$$C_{\text{PI-LPF}}(s) = \frac{K_P \omega_{\text{lpf}}(s + K_I/K_P)}{s(s + \omega_{\text{lpf}})}, \quad (18)$$

TABLE II: Controller parameters.

| Controller | K_P [rad/Nm] | K_I [rad ² /(Nms)] | ω_{lpf} [rad/s] |
|-----------------------|----------------|---------------------------------|-------------------------------|
| C_{I_1} | - | 7.9e-10 | - |
| $C_{\text{PI-LPF}_1}$ | 1.1e-8 | 1.34e-11 | 1 |
| $C_{\text{PI-LPF}_2}$ | 1.1e-8 | 1.32e-11 | 0.0718 |
| C_{I_2} | - | 1.34e-11 | - |

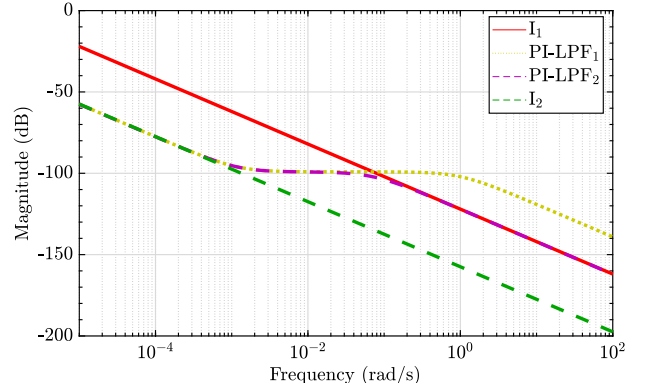


Fig. 5: Comparison of the Bode plots of the different controller types.

where the chosen tuning parameters are provided in Table II and the resulting Bode plots of the controllers are given in Fig. 5.

Since only a bias is corrected, an integral controller (17) may already be sufficient as it corrects the steady-state error. Two different gains are examined here to compare different levels of aggressiveness. However, if the error signal contains too rapid changes, possibly due to non-ideal conditions such as turbulence or gusts, a PI controller may respond better to the immediate error. Nevertheless, this may increase actuator costs due to the high-frequency content included in the control action. Thus, a trade-off between smooth control performance and actuator activity may be accommodated by the PI-LPF controller (18), which is evaluated here for different combinations between the K_I , K_P , and ω_{lpf} parameters. The resulting Helix frame loop transfers in the discrete-time domain with zero-order hold discretization method where sampling time $dt = 0.005$ s is used, is shown in Fig. 6.

Note that these controllers are not fully optimized and selected to study the effect of different controller concepts. More advanced controller synthesis may yield better performance and is the subject of future work.

V. SIMULATION SETUP

The effectiveness of the controllers is studied in a high-fidelity simulation environment, where the aero-hydro-servo-elastic wind turbine tool OpenFAST (Fatigue, Aerodynamics, Structures, and Turbulence) [23] is coupled to the high-fidelity fluids solver Adaptive Mesh Refinement (AMR)-Wind to perform coupled LES. This section introduces these codes and presents the simulation settings used in this study.

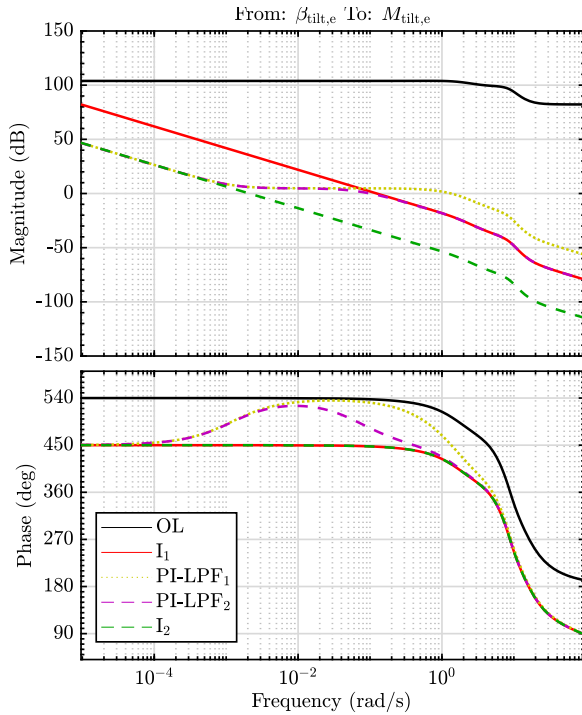


Fig. 6: Comparison of the different loop transfers including different controller types. OL denotes the open-loop system.

A. OpenFAST simulation setup

OpenFAST is a multi-fidelity wind turbine simulation tool coupling several standalone modules relating to different aspects of wind turbine simulation, including the structural dynamics, control system, hydrodynamic, and aerodynamics loads. The aerodynamic loads can be computed through computationally efficient engineering models such as the blade element momentum (BEM) theory model, or higher-fidelity models such as free-vortex methods or flow solvers like AMR-Wind.

The current work evaluates the proposed controllers on the International Energy Agency’s (IEA) 15 MW fixed-bottom reference wind turbine [24]. This turbine is controlled using the reference open-source controller (ROSCO) [25], which is modified to include the proposed control scheme². Some specifications of this turbine are given in Table III.

The OpenFAST simulation is coupled to the LES through the actuator line method (ALM) [26], where the turbine blades are represented as lines composed of discrete segments along their span. Each segment is associated with an ‘actuator’, which is a mathematical representation of the forces applied by that part of the blade on the fluid. These forces influence the local flow conditions, such as velocity, pressure, and turbulence.

Even though the actuator line method allows more computationally efficient LES, the simulation requires significant resources and runs at a time step of 0.05 seconds while the OpenFAST simulation runs at a smaller time step of 0.005 seconds where interpolation is performed to facilitate the data exchange. Note that the interpolation in coupled LES

TABLE III: Specifications of the IEA 15 MW reference turbine.

| Characteristic | Value |
|--------------------|-----------|
| Hub height | 150 m |
| Rotor diameter | 240 m |
| Rated power | 15 MW |
| Rated wind speed | 10.59 m/s |
| Cut-in wind speed | 3 m/s |
| Cut-out wind speed | 25 m/s |
| Min. rotor speed | 5 rpm |
| Max. rotor speed | 7.56 rpm |

introduces phase lags to the controller which increase the optimal azimuth offset. An additional phase correction may be necessary to fully decouple the pitch control system ensuring optimal controller performance [22].

B. AMR-Wind simulation setup

AMR-Wind is a parallel adaptive-mesh solver for incompressible flow built on the AMReX library and specifically targeted for wind energy [27]. The software enables LES of atmospheric boundary layer flows, wind farm turbine-wake interactions, and blade-resolved simulations of multiple turbines within a wind farm and is therefore very suited for evaluating controllers that rely on the interaction between wind turbines, such as the controller proposed in this paper. For details regarding the governing equations and wall models of AMR-Wind, the reader is referred to [28].

In this work, and similar to previous work [10], a Convective Boundary Layer (CNBL) precursor including Coriolis force effects is investigated, where the Atmospheric Boundary Layer (ABL) interacts with a stable stratified free atmosphere characterized by a lapse rate of 1 K/km. As recommended in [29], a capping inversion is employed to control the growth and height, where the boundary layer height (h) is set at 1000 m, with a surface roughness (z_0) of 0.0002 m based on offshore measurements in the Netherlands [30].

For the precursor simulation, the domain size is $x = 5360$ m, $y = 3200$ m, $z = 1600$ m, accommodating three turbines. The isotropic grid size is 10 m, meeting CNBL requirements [31]. Using periodic boundary conditions, the flow evolves for 16 hours, establishing a quasi-stationary turbulent ABL state [32].

Subsequently, during the next 45 minutes, y-z planes are sampled at the inflow ($x = 0$ m) as inflow boundary conditions for turbine simulations. These simulations are enabled through the ALM coupling with OpenFAST.

In the domain, the three turbines are placed at ($x = 1200$ m, $y = 1600$ m), ($x = 2400$ m, $y = 1600$ m), and ($x = 3600$ m, $y = 1600$ m), for turbine 1 (T1), T2, and T3, respectively, accommodating a 5D spacing from the inflow and a 5D spacing between the turbines, while leaving sufficient space for the wake behind the third turbine to develop.

A mesh refinement to 5 m is set surrounding the three turbines in a static box with size $x_m = 5040$ m, $y_m = 960$ m, $z_m = 600$ m starting 4.5D upstream of the first turbine to enable higher resolution flow surrounding the wind turbines. A snapshot for illustration of one LES is given in Fig. 7. Note

²<https://github.com/mvanv/ROSCO/tree/WakeMixingLoadIPC>

TABLE IV: Overview of the controllers used in each test case.

| Case | T1 | T2 | T3 | Ref. [kNm] |
|----------|-----------|--|--------|------------|
| BL Helix | CCW Helix | Greedy | Greedy | n.a. |
| TC1 | CCW Helix | I_1 -Rej. | Greedy | n.a. |
| TC2 | CCW Helix | PI-LPF ₁ -Rej. | Greedy | n.a. |
| TC3 | CCW Helix | PI-LPF ₂ -Rej. | Greedy | n.a. |
| TC4 | CCW Helix | I_2 -Rej. | Greedy | n.a. |
| TC5 | CCW Helix | I_1 -Track. | Greedy | 1e4 |
| TC6 | CCW Helix | PI-LPF ₁ -Track. | Greedy | 1e4 |
| TC7 | CCW Helix | PI-LPF ₂ -Track. | Greedy | 1e4 |
| TC8 | CCW Helix | I_2 -Track. | Greedy | 1e4 |
| TC9 | CCW Helix | PI-LPF ₁ ⁺ -Track. | Greedy | 1.2e4 |

the highly resolved flow showing wake characteristics such as meandering due to the Helix actuation strategy.

Each LES is run on the supercomputer DelftBlue [33] and is run parallelized on 528 processors with 4GB of memory each. The total real-time duration of each simulation is approximately 48 hours.

C. Test cases

To study the effect of the proposed control scheme on the loads and power production, ten coupled LES are performed (Table IV). A baseline Helix case is performed where a CCW Helix with 4-degree amplitude and $S_t = 0.25$ is initiated on the first turbine, while the second and third operate with their baseline ‘greedy’ control strategy. These specific Helix settings were chosen to comply with the original settings from [9] but may be further optimized as desired. The first four test cases evaluate the rejection control strategy to drive the Helix load to zero using the controllers described in Table II. The next four test cases evaluate the tracking control strategy using the same controller types, where a reference $M_e^{\text{ref}} = 1\text{e}4\text{ kNm}$ is set, which is double the value it attains during the baseline case. Note that this reference value is not optimized here to maximize a power/loads trade-off due to the computational cost of LES. However, a single test case with an increased amplitude reference $M_e^{\text{ref}} = 1.2\text{e}4\text{ kNm}$ is run, which is analyzed in terms of power and loads.

VI. RESULTS: REJECTION SCHEME

This section presents the findings of the investigation into the rejection scheme’s performance by evaluation of TC1-TC4 which employ different PID-type controllers. The analysis encompasses evaluating the controller’s rejection performance, assessment of the required pitch actuator actions, and analysis of the damage-equivalent loads (DELs) per industry practice.

A. Analysis of controller performance

Here, the controller performance is evaluated by investigating the system response in both the frequency and time domain.

Figure 8 displays the rotor loads in different reference frames, with M_1 in the rotating frame, M_{ilt} in the fixed frame, and $M_{\text{ilt},e}$ in the Helix frame³. The left column shows the

frequency-domain representation of these signals, in the form of a power spectrum, while the right column presents low-pass filtered time series data.

The objective of the rejection controller is to drive the Helix load towards zero. In the frequency domain plots, this can be observed by inspecting the Helix load in the different reference frames. Note that the Helix and wind-induced rotor-asymmetric load appear at different locations in the different frames (see Table I). A clear difference is notable between the aggressiveness of the controllers, where the I_2 controller shows much less attenuation compared to e.g. the I_1 controller.

In the time domain, this difference in aggressiveness becomes clear as well, where it can be seen that most controllers successfully drive the bias in $M_{\text{ilt},e}$ towards zero, while the I_2 controller only slightly appears to do so.

Interestingly, the wind-induced rotor asymmetric load appears to be reduced by the controllers as well, benefiting the fatigue life even more. Note that the less aggressive I_2 controller does not attenuate this load. This observation is also clearly visible in the rotating frame, where this load appears at the $1P$ frequency.

To further understand the reason why some controllers correct the wind-induced rotor asymmetric load as well, the sensitivity function of the $\beta_{\text{tilt},e}$ to $M_{\text{ilt},e}$ transfer in the Helix frame is studied in Fig. 9. The sensitivity function is given by:

$$\frac{1}{1 + G(s)C(s)}, \quad (19)$$

This function provides insights into the controller’s effectiveness across various frequencies. The objective is to maintain a consistent gain of 0dB across all frequencies while attenuating the DC gain, where the Helix load acts in the Helix coordinate frame. In this figure, it becomes evident that the controllers adeptly mitigate lower frequencies, aligning with the desired behavior. However, a closer observation reveals that the I_1 -, PI-LPF₁, and PI-LPF₂-controllers introduce some attenuation to f_e , which explains the behavior of these controllers in reducing the wind-induced rotor asymmetric load.

It should be noted that the control settings and tuning significantly impact the controller’s performance. For example, if a large Strouhal number is selected, the wind-induced rotor asymmetric load is at a significantly higher frequency in the Helix frame, which might not be attenuated by any of the current controllers. Or, if different gains are chosen, the region of attenuation may become smaller or larger. Therefore, if the objective is to reduce both the wind-induced rotor asymmetric load and Helix load, a careful methodology should be followed to ensure both are mitigated as desired. Possibly more advanced H_2 - or H_∞ -control could provide more effective solutions (see e.g. [34]).

In summary, the load rejection scheme effectively mitigates the Helix load in most control setups while also attenuating the wind-induced rotor asymmetric load in the most aggressive controllers, as demonstrated by both time and frequency domain analyses. These results show promising indications for enhancing the fatigue life of the downstream turbine which is further analyzed in the next section by quantifying the DELs.

³As the conclusions drawn from the results of the orthogonal channels (yaw, yaw_e) and blade 2 and 3 are similar, they are omitted in the remainder of this paper for conciseness but available upon request.

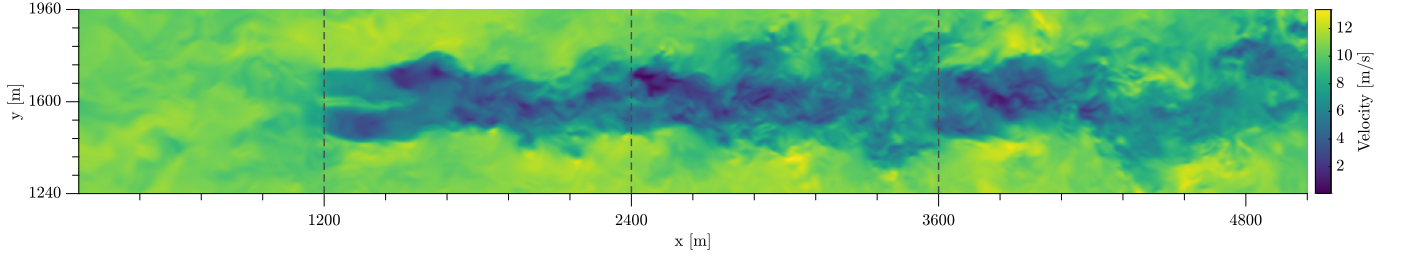


Fig. 7: Vertical slice of the static box refinement at $t = 59800$ s showing velocity in the x direction for Test Case 6. The turbines are placed at the dashed lines.

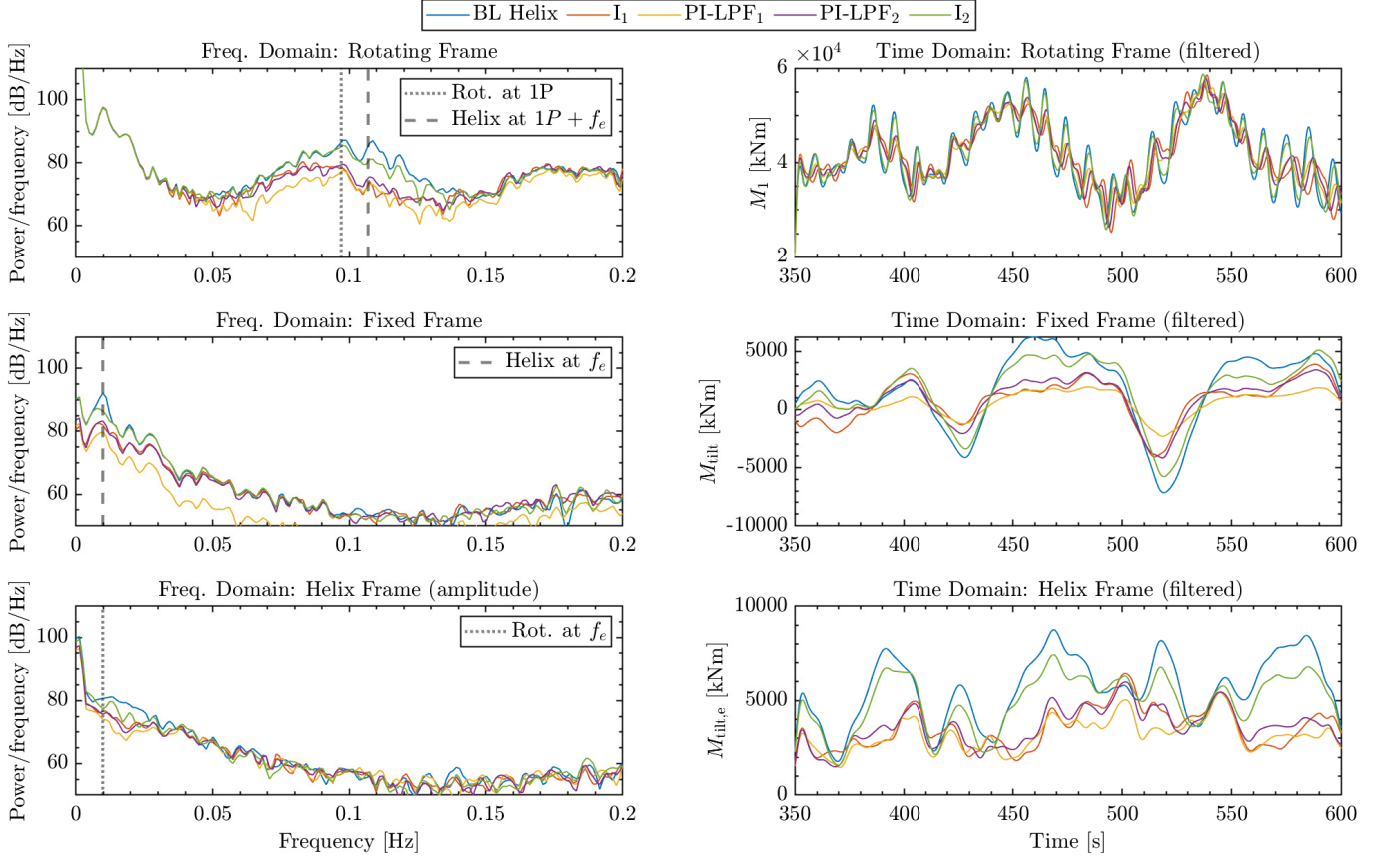


Fig. 8: Comparison of the blade loads of T2 in different reference frames in the frequency domain.

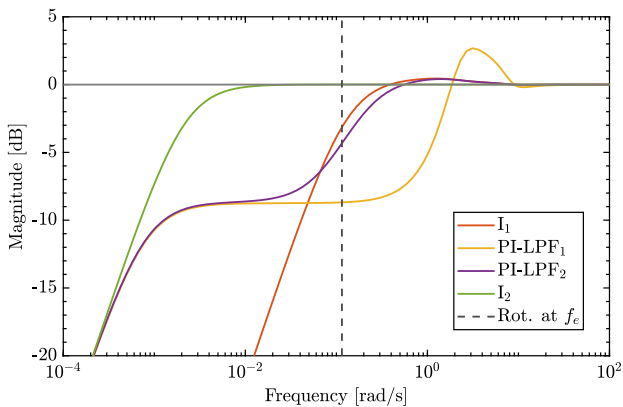


Fig. 9: Sensitivity function of the rejection controller.

B. Impact on power production, DELs, and PBD

This section quantifies the improvement of the fatigue life of T2 and T3 due to the proposed controller by computation of the DELs and comparison against the baseline Helix case. This metric allows a comparison of the degree of loading a turbine encounters during simulation and complies with the industry convention according to the IEC-61400 standard [35]. It further relies on the rainflow counting algorithm and is computed through the following formula:

$$\text{DEL} = \left(\frac{\sum_{i=1}^N (A_i)^m n_i}{n_{eq}} \right)^{\frac{1}{m}}, \quad (20)$$

where N is the total count of cycles, m is the inverse Wöhler slope, conventionally taken as 5 for steel tower components and 10 for composite blade structures. Moreover, n_i indicates

TABLE V: Overview of the power of the different controllers.

| Controller | T2 [MW] | T3 [MW] | T2+T3 [MW] |
|--------------------------------|---------------|---------------|----------------|
| I ₁ -rejection | 6.93 (-1.83%) | 6.77 (-1.27%) | 13.71 (-1.56%) |
| PI-LPF ₁ -rejection | 6.99 (-1.06%) | 6.88 (+0.23%) | 13.86 (-0.42%) |
| PI-LPF ₂ -rejection | 6.97 (-1.30%) | 6.84 (-0.28%) | 13.81 (-0.80%) |
| I ₂ -rejection | 7.03 (-0.54%) | 6.85 (-0.20%) | 13.87 (-0.37%) |

the number of cycles represented by a range of A_i , and n_{eq} denotes the equivalent cycle, set to 1 here.

The first 350 seconds of the dataset are discarded to account for the propagation of the wake from the upstream to the downstream turbine and other transient effects in the simulation. A total of 2150 seconds of simulation time are used in the DEL calculations.

Figures 10b and 10c show the results of the DEL calculations, where the DEL of the controllers is displayed relative to the baseline Helix case. It is evident from the bar graph that there are significant disparities in the reduction in loads between the different controllers. All controllers show a substantial decrease in DEL. However, this reduction does not come without costs, as the I₁-controller causes a notable reduction in power, and others also see a slight power decrease (Fig. 10a and Table V). The I₂ and PI-LPF₁ appear to strike the best balance between load reduction and power production preservation.

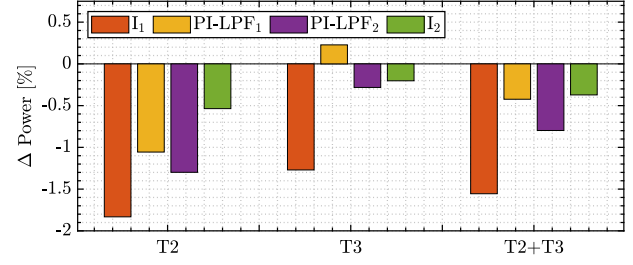
Interestingly, also the third turbine experiences substantial load reductions for most controllers. Even for the case where the third turbine experiences a small power gain, with the PI-LPF₁ and I₂ controllers, there is a load reduction visible on the third turbine, while usually an increase in power is associated with a DEL increase.

Another metric used to study fatigue is pitch bearing damage (PBD). This is damage that builds up in the pitch actuators over time and can be understood as the cost of the control action that is required to achieve the control objective. The formula is given by [20]:

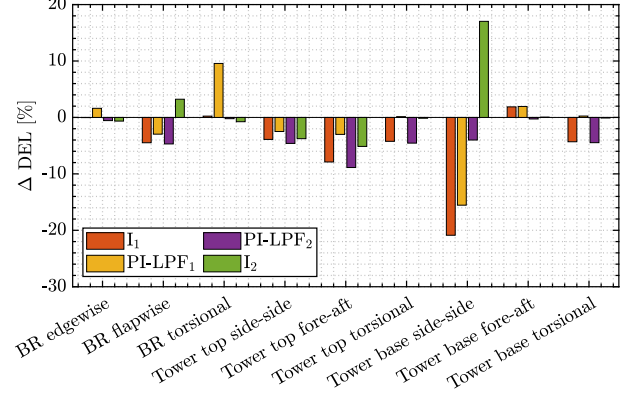
$$\text{PBD}(\gamma) = \sum_{k=1}^N \delta\theta(k) (\max(\cos(\gamma)M_{\text{flap}}(k) + \sin(\gamma)M_{\text{edge}}(k), 0))^m, \quad (21)$$

where γ is the radial position of the bearing, $\delta\theta$ is the pitch difference, M_{flap} is the flapwise blade root moment, M_{edge} is the edgewise blade root moment, and m is the inverse Wöhler slope. Here, only the radial position with the largest damage is examined.

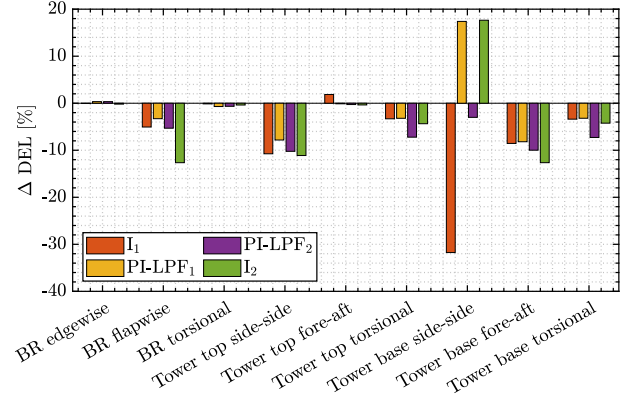
The computed PBDs are displayed in Table VI, which are compared against the PBD of T1. It can be observed that the PBD of T1 is very high compared to the PBD of T2 employing the rejection controllers while actuating with similar pitch amplitude and frequency. The strong difference in wind speed increasing the blade root moment on T1 plays a role here, but another important cause is the reduction in the blade root moment on T2 as a result of the I₁-rejection controller. Observe in (21) that it is a function of the blade root moments. Even though significant pitch action is required, a reduction of blade root moment prevents a substantial increase in PBD



(a) Bar chart of the power difference relative to the baseline Helix case for both T2, T3, and combined.



(b) Bar chart of the damage-equivalent loads of the rejection controllers relative to the baseline Helix case for T2. 'BR' denotes blade root.



(c) Bar chart of the damage-equivalent loads of the rejection controllers relative to the baseline Helix case for T3. 'BR' denotes blade root.

Fig. 10: Performance plots of the rejection controllers.

on T2, significantly alleviating PBD concerns regarding the implementation of this method.

Finally, the vertical mean streamwise velocity profile in the wake of T2 comparing baseline Helix against the I₁- and PI-LPF₂-rejection controller is investigated. In Fig. 11, it can be observed that the wake recovery of the baseline Helix case and PI-LPF₂ case is slightly better compared to the I₁-rejection controller, explaining the power loss as a result of the pitching strategy.

TABLE VI: Overview of the PBDs of the different controllers.

| Turbine | Controller | PBD ($\times 10^{17}$) |
|---------|--------------------------------|--------------------------|
| T1 | BL Helix | 20.17 |
| T2 | I_1 -rejection | 0.78 |
| | PI-LPF ₁ -rejection | 1.76 |
| | PI-LPF ₂ -rejection | 0.63 |
| | I_2 -rejection | 0.52 |

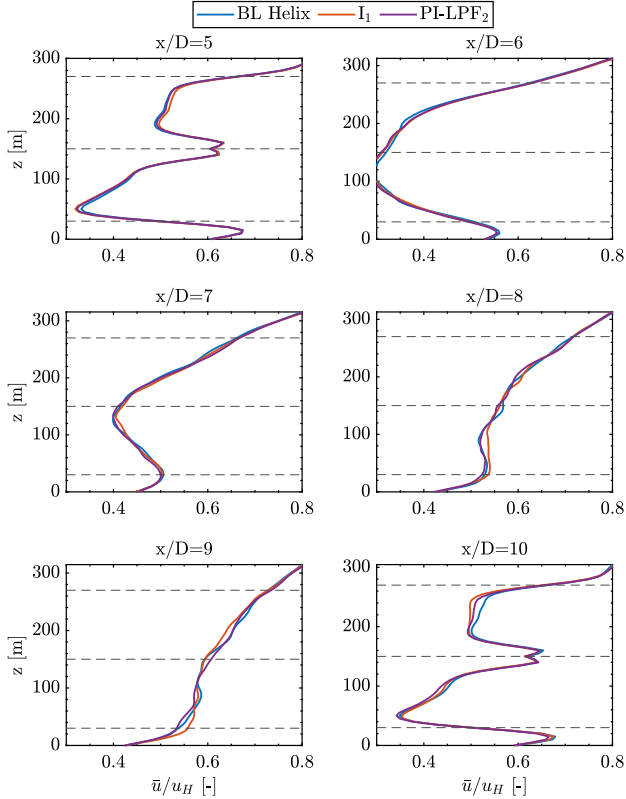


Fig. 11: Vertical mean streamwise velocity profile of the wake behind T2 for several rotor distances D behind T2 ($x/D = 5$). T3 is located at $x/D = 10$.

VII. RESULTS: TRACKING SCHEME

After discussion of the results of the rejection scheme, this section now presents the results obtained when toggling the other objective—synchronized wake mixing for power enhancement, which is achieved by tracking a reference. Here TC5 - TC9 are evaluated and compared, where the tracking performance of the controller, DELs, and PBD are analyzed. Also, some flow analysis is presented and reviewed.

A. Analysis of controller performance

This section examines the controller performance by performing time and frequency domain investigations of the system's response and control commands.

Figure 12 displays the rotor loads in different reference frames, with M_1 in the rotating frame, M_{tilt} in the fixed frame, and M_e in the Helix frame. Rather than analyzing $M_{\text{tilt},e}$ and $M_{\text{yaw},e}$, the control performance is better understood when inspecting the amplitude M_e since the phase ϕ_e of $M_{\text{tilt},e}$ and $M_{\text{yaw},e}$ might change over time. This influences the resulting

reference to $M_{\text{tilt},e}$ and $M_{\text{yaw},e}$ and makes drawing conclusions in the time domain more challenging. The left column shows the frequency domain representation of these signals, in the form of a power spectrum, while the right column presents low-pass filtered time series data.

The objective of the tracking controller is to correct the bias to the reference M_e^{ref} , essentially amplifying the Helix frequency. This amplification can be observed in the frequency domain, where the characteristic peak has increased in the rotating and fixed coordinate frame. In the time domain, an interesting observation of the phase synchronization capabilities can be made, where it appears in the fixed frame in Fig. 12 that the aggressive I_1 controller is not able to match the phase with the baseline Helix case's phase. This implies it does not fully leverage the already present content and needs to compensate to force a different phase in the response requiring more pitch action.

The PI-LPF₁-controller, while synchronizing the phase, has a rather noisy pitch signal which can be seen from Fig. 13, which depicts the pitch rate. A noisy pitch signal impacts loads on the structure and damages the pitch bearing. Ultimately, the PI-LPF₂-controller may be considered to show a compromise between the aggressiveness of the I_1 -controller and the desired control behavior, as shown by the PI-LPF₁-controller. Akin to the PI-LPF₁-controller, it can synchronize but does not exercise a high-frequent pitch signal, making it a suitable candidate for the phase-synchronization objective. A target sensitivity Bode plot could be established, demonstrating the suitability of this approach for H_2/H_∞ controller synthesis. The next section quantifies the DELs and PBDs and studies the power production of the test cases.

B. Impact on power production, DELs, and PBD

Here, the impact on the fatigue life, pitch bearing, and power production is studied. Also, an additional test case, namely PI-LPF₁⁺, is examined, in which an increased reference M_e^{ref} is used. Since the objective is phase synchronization for power enhancement, first, the power production of each control case is investigated in Fig. 14a. The I_1 -tracking controller appears to cause a significant power loss on T2, which may be caused by the inability to fully exploit the periodic wake such that phase synchronization could not always be attained. However, a power increase is observable at T3 as a result of the tracking controller on T2, although it is insufficient to increase the aggregate power capture of both turbines.

Interestingly, a substantial power gain can be observed on T2 when employing the other controllers, which suggests that baseline greedy control is not optimal for power extraction when a turbine is in a Helix wake. Even more striking is the fact that, due to phase synchronization, the wake mixing is continued further downstream and significantly benefits T3 as a significant power gain of 4.39% could be attained for the PI-LPF₁-controller, resulting in a 2.3% overall power gain underlining the potential of phase synchronized wake mixing. Similarly, the PI-LPF₂ controller shows a power increase, with a considerable power gain of 3.98% on T3, while increasing the total power with 2.01%. The best performing controller

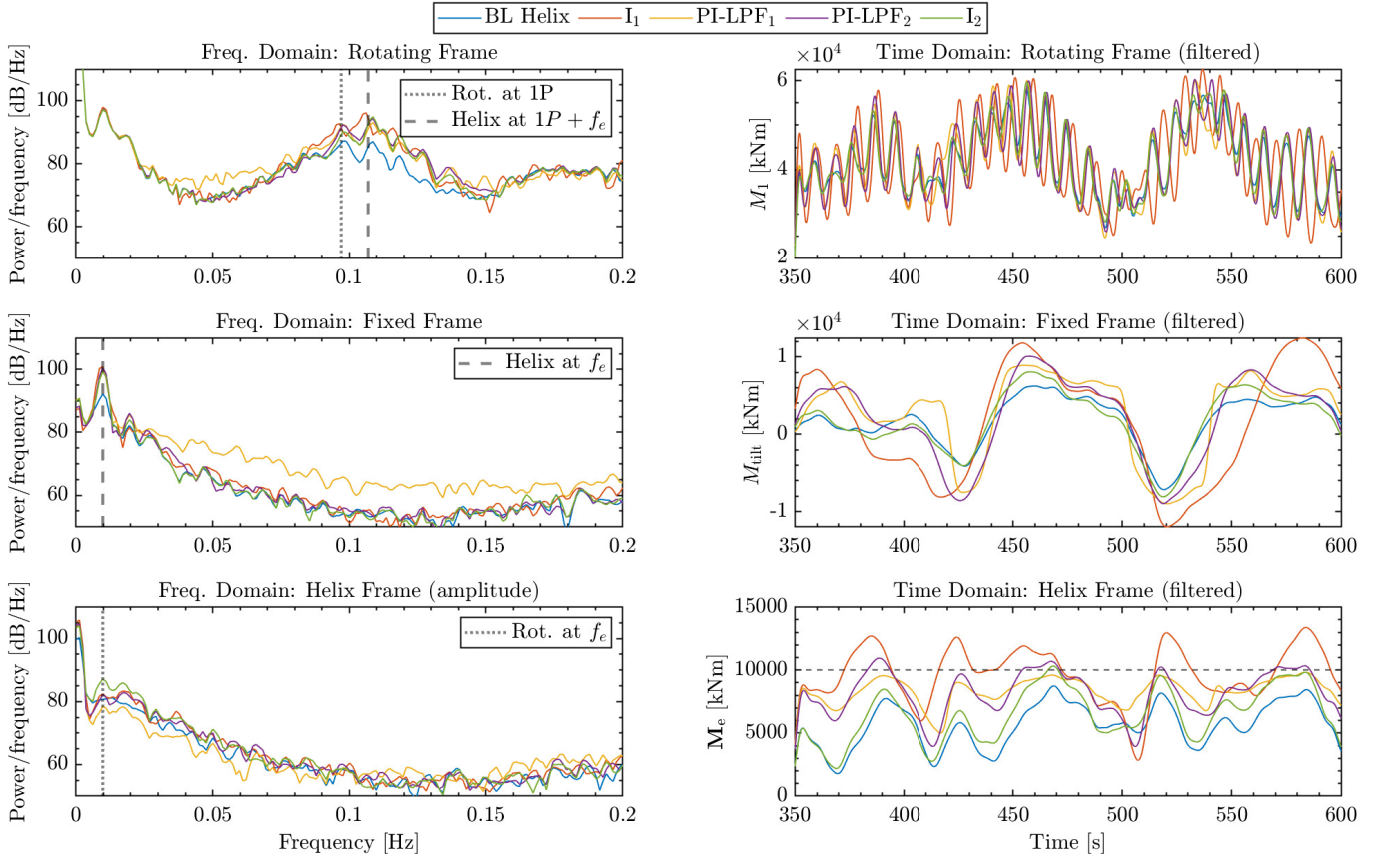


Fig. 12: Comparison of the blade loads of T2 in different reference frames in the frequency domain.

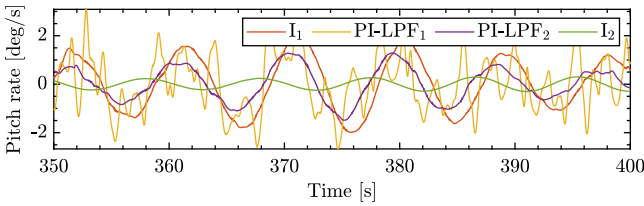


Fig. 13: Comparison of the pitch rate.

TABLE VII: Overview of the power of the different controllers.

| Controller | T2 [MW] | T3 [MW] | T2+T3 [MW] |
|--|---------------|---------------|----------------|
| I ₁ -tracking | 6.81 (-3.58%) | 6.89 (+0.50%) | 13.70 (-1.57%) |
| PI-LPF ₁ -tracking | 7.08 (+0.26%) | 7.16 (+4.39%) | 14.24 (+2.30%) |
| PI-LPF ₂ -tracking | 7.07 (+0.09%) | 7.13 (+3.98%) | 14.20 (+2.01%) |
| I ₂ -tracking | 7.07 (+0.17%) | 6.96 (+1.43%) | 14.03 (+0.79%) |
| PI-LPF ₁ ⁺ -tracking | 7.07 (+0.05%) | 7.27 (+5.96%) | 14.34 (+2.96%) |

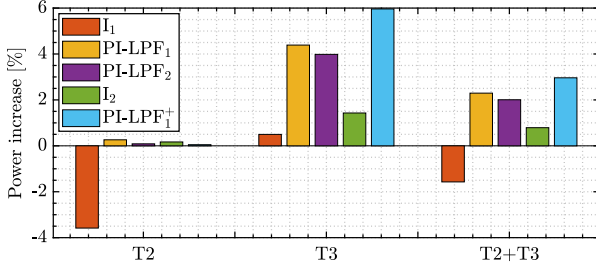
PI-LPF₁ was tested with an extended reference referred to as the case PI-LPF₁⁺, where an even more prominent power increase of 5.96% could be observed on T2 and a collective increase of 2.96%. An overview of the power production for each controller is given in Table VII.

Next, an analysis is made of the DEL increase for all cases relative to baseline in Fig. 14b for T2 and Fig. 14c for T3. From Fig. 14b, it can be concluded that all cases increase the DELs on T2, while the strongest increase is in the I₁-tracking

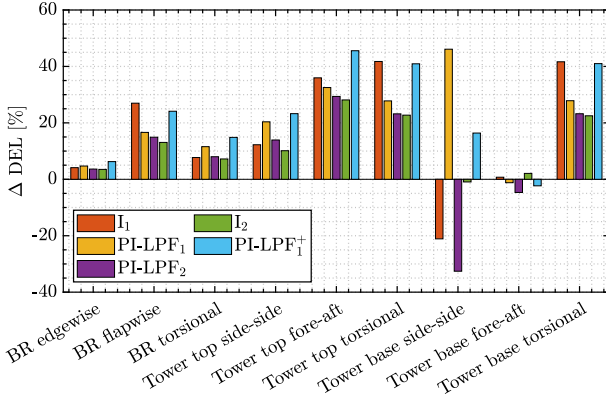
case. For example, the strong increase in DEL on the blade root flapwise moment for the I₁-tracking controller is due to the stronger amplification, while the increases of the PI-LPF₁-controller are due to the large variations in the pitch actuation, where higher frequent noise propagates to the turbine structure and increases the fatigue damage. In the case of T3, there are no clear trends visible. Generally, when the wind speed is higher due to wake mixing, a slight load increase may be expected on T3, this is, however, not yet conclusive and would require more extensive load studies, e.g. by averaging results from various turbulence realizations [35]. In summary, the PI-LPF₁-, PI-LPF₂-, or I₂-tracking controllers appear to be the optimal scheme in terms of DEL.

Furthermore, the PBDs of the different control schemes are presented in Table VIII. Here, the hypothesis of the analysis in Section VII-B is confirmed. Due to the more extensive pitch variations in the PI-LPF₁-tracking case, the resulting PBD is slightly higher and impacts the fatigue life of the bearing more than for the other cases, where lower PBDs are found. Nonetheless, the highest PBD is found for the I₁-controller, which requires more pitching to track the reference as it does not seem to fully exploit periodic the content already present in the wake. The I₂ controller exhibits the lowest PBD, as it is the least aggressive controller. The reason for a high PBD for the PI-LPF₁⁺ case is due to the extended M_e^{ref} value, although it is still very reasonable.

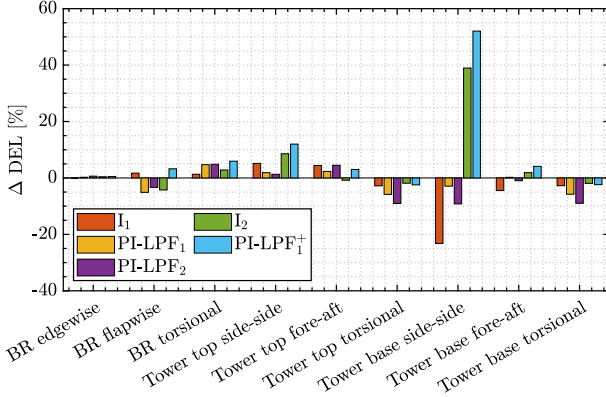
Finally, the vertical mean streamwise velocity profile in the



(a) Bar chart of the power increase relative to the baseline Helix case for both T2, T3, and combined.



(b) Bar chart of the DEL increase relative to the baseline Helix case for T2 for the different controllers.



(c) Bar chart of the DEL increase relative to the baseline Helix case for T3 for the different controllers.

Fig. 14: Performance plots of the tracking controllers.

TABLE VIII: Overview of the PBDs of the different controllers.

| Turbine | Controller | PBD ($\times 10^{17}$) |
|---------|------------------------|--------------------------|
| T1 | BL Helix | 20.17 |
| T2 | I_1 -tracking | 2.23 |
| | $PI-LPF_1$ -tracking | 1.88 |
| | $PI-LPF_2$ -tracking | 1.36 |
| | I_2 -tracking | 1.09 |
| | $PI-LPF_1^+$ -tracking | 2.28 |

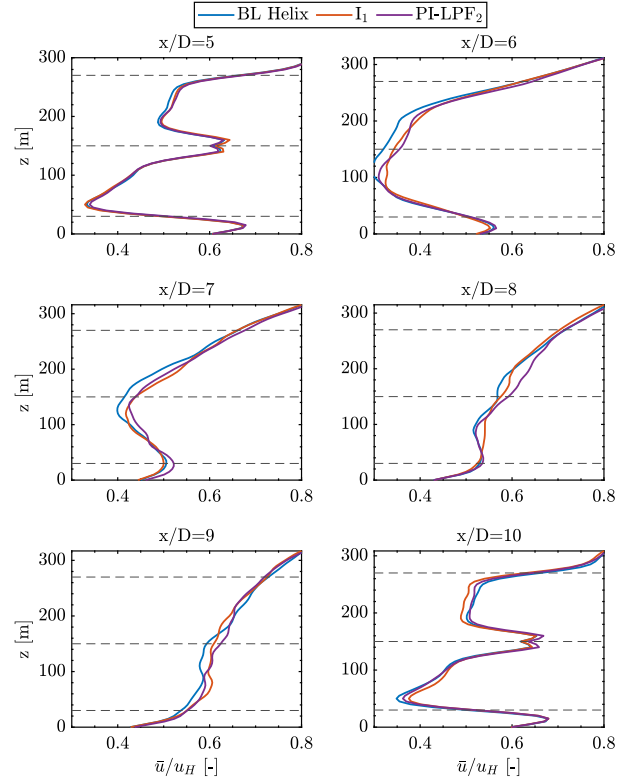


Fig. 15: Vertical mean streamwise velocity profile of the wake behind T2 for several rotor distances D behind T2 ($x/D = 5$). T3 is located at $x/D = 10$.

wake of T2 is analyzed in this section. Figure 15 showcases these results, where a comparison is made against the baseline case across several rotor diameters behind T2 up to T3 for only the I_1 and $PI-LPF_2$ controller (for clarity's sake). The wake recovery of the $PI-LPF_2$ -tracking controller appears superior to the I_1 case, which explains the strong performance gain on T3 compared to the other methods.

VIII. CONCLUSION

This study examined downstream turbine control in a Helix wake, proposing two strategies: load rejection and phase synchronization. A novel extension of the multi-blade coordinate transformation was proposed, enabling the use of linear PID-type controllers to execute both strategies. Computational simulations incorporating three turbines demonstrated promising results: load rejection improved turbine fatigue life by up to 10%, while phase synchronization led to a 6% power gain on T3 compared to the baseline Helix setup. Further optimization and exploration of advanced control strategies employing this coordinate transformation are recommended, as further power improvements are expected.

ACKNOWLEDGEMENT

This work is part of the Hollandse Kust Noord wind farm innovation program where CrossWind C.V., Shell, Grow, Eneco, and Siemens Gamesa are teaming up; funding for the PhDs was provided by CrossWind C.V. and Siemens Gamesa. We

further acknowledge the computational resources provided by DelftBlue [33].

REFERENCES

- [1] F. González-Longatt, P. Wall, and V. Terzija, “Wake effect in wind farm performance: Steady-state and dynamic behavior,” *Renewable Energy*, vol. 39, no. 1, pp. 329–338, 2012.
- [2] R. J. Barthelmie, K. Hansen, S. T. Frandsen, O. Rathmann, J. Schepers, W. Schlez, J. Phillips, K. Rados, A. Zervos, E. Politis, *et al.*, “Modelling and measuring flow and wind turbine wakes in large wind farms offshore,” *Wind Energy*, vol. 12, no. 5, pp. 431–444, 2009.
- [3] J. Annoni, P. M. Gebraad, A. K. Scholbrock, P. A. Fleming, and J. W. van Wingerden, “Analysis of axial-induction-based wind plant control using an engineering and a high-order wind plant model,” *Wind Energy*, vol. 19, no. 6, pp. 1135–1150, 2016.
- [4] D. C. van der Hoek, S. Kanev, J. Allin, D. Bieniek, and N. Mittelmeier, “Effects of axial induction control on wind farm energy production—a field test,” *Renewable energy*, vol. 140, pp. 994–1003, 2019.
- [5] P. A. Fleming, P. M. Gebraad, S. Lee, J. W. van Wingerden, K. Johnson, M. Churchfield, J. Michalakes, P. Spalart, and P. Moriarty, “Evaluating techniques for redirecting turbine wakes using sowfa,” *Renewable Energy*, vol. 70, pp. 211–218, 2014.
- [6] J. P. Goit and J. Meyers, “Optimal control of energy extraction in wind-farm boundary layers,” *Journal of Fluid Mechanics*, vol. 768, pp. 5–50, 2015.
- [7] J. A. Frederik, R. Weber, S. Cacciola, F. Campagnolo, A. Croce, C. Bottasso, and J. W. van Wingerden, “Periodic dynamic induction control of wind farms: proving the potential in simulations and wind tunnel experiments,” *Wind Energy Science*, vol. 5, no. 1, pp. 245–257, 2020.
- [8] J. A. Frederik and J. W. van Wingerden, “On the load impact of dynamic wind farm wake mixing strategies,” *Renewable Energy*, 2022.
- [9] J. A. Frederik, B. M. Doekemeijer, S. P. Mulders, and J. W. van Wingerden, “The helix approach: Using dynamic individual pitch control to enhance wake mixing in wind farms,” *Wind Energy*, vol. 23, no. 8, pp. 1739–1751, 2020.
- [10] E. Taschner, A. A. W. van Vondelen, R. Verzijlbergh, and J. W. van Wingerden, “On the performance of the helix wind farm control approach in the conventionally neutral atmospheric boundary layer,” in *Journal of Physics: Conference Series*, vol. 2505, p. 012006, IOP Publishing, 2023.
- [11] D. C. van der Hoek, B. V. d. Abbelee, C. S. Ferreira, and J. W. van Wingerden, “Maximizing wind farm power output with the helix approach—experimental validation and wake analysis using tomographic piv,” *arXiv preprint arXiv:2306.12849*, 2023.
- [12] L. J. Huang, S. P. Mulders, E. Taschner, and J. W. van Wingerden, “Enhancing wake mixing in wind farms by multi-sine signals in the helix approach,” in *2023 American Control Conference (ACC)*, pp. 824–830, IEEE, 2023.
- [13] H. Korb, H. Asmuth, and S. Ivanell, “The characteristics of helically deflected wind turbine wakes,” *Journal of Fluid Mechanics*, vol. 965, p. A2, 2023.
- [14] A. A. W. van Vondelen, J. Ottenheim, A. K. Pamososuryo, S. T. Navalkar, and J. W. van Wingerden, “Phase synchronization for helix enhanced wake mixing in downstream wind turbines,” *IFAC-PapersOnLine*, vol. 56, no. 2, pp. 8426–8431, 2023.
- [15] E. A. Bossanyi, “Individual blade pitch control for load reduction,” *Wind Energy: An International Journal for Progress and Applications in Wind Power Conversion Technology*, vol. 6, no. 2, pp. 119–128, 2003.
- [16] A. V. Oppenheim, A. S. Willsky, S. H. Nawab, and J.-J. Ding, *Signals and systems*, vol. 2. Prentice hall Upper Saddle River, NJ, 1997.
- [17] E. van Solingen and J. W. van Wingerden, “Linear individual pitch control design for two-bladed wind turbines,” *Wind Energy*, vol. 18, no. 4, pp. 677–697, 2015.
- [18] S. P. Mulders, A. K. Pamososuryo, G. E. Disario, and J. W. van Wingerden, “Analysis and optimal individual pitch control decoupling by inclusion of an azimuth offset in the multiblade coordinate transformation,” *Wind Energy*, vol. 22, pp. 341–359, Mar. 2019.
- [19] A. K. Pamososuryo, S. P. Mulders, R. Ferrari, and J. W. van Wingerden, “On the analysis and synthesis of wind turbine side-side tower load control via demodulation,” *arXiv preprint arXiv:2309.01633*, 2023.
- [20] A. A. W. van Vondelen, S. T. Navalkar, D. R. H. Kerssemakers, and J. W. van Wingerden, “Enhanced wake mixing in wind farms using the helix approach: A loads sensitivity study,” in *2023 American Control Conference (ACC)*, pp. 831–836, IEEE, 2023.
- [21] G. Van der Veen, J. W. van Wingerden, M. Bergamasco, M. Lovera, and M. Verhaegen, “Closed-loop subspace identification methods: an overview,” *IET Control Theory & Applications*, vol. 7, no. 10, pp. 1339–1358, 2013.
- [22] A. A. W. van Vondelen, A. K. Pamososuryo, S. T. Navalkar, and J. W. van Wingerden, “On the optimal azimuth offset for individual pitch control in aeroelastic code coupled with a high-fidelity flow solver,” in *Submitted to: 2024 European Control Conference (ECC)*, IEEE, 2024.
- [23] B. Jonkman, R. M. Mudafort, A. Platt, E. Branlard, M. Sprague, J. Jonkman, H. Ross, M. Hall, G. Vijayakumar, M. Buhl, P. Bortolotti, S. Ananthan, and J. Rood, “OpenFAST/openfast: OpenFAST v3.4.0,” Zenodo, Jan. 2023.
- [24] E. Gaertner, J. Rinker, L. Sethuraman, F. Zahle, B. Anderson, G. E. Barter, N. J. Abbas, F. Meng, P. Bortolotti, W. Skrzypinski, *et al.*, “Iea wind tcp task 37: definition of the IEA 15-megawatt offshore reference wind turbine,” tech. rep., National Renewable Energy Lab.(NREL), Golden, CO (United States), 2020.
- [25] N. J. Abbas, D. Zalkind, R. M. Mudafort, G. Hylander, S. Mulders, D. Heff, and P. Bortolotti, “Nrel/rosco: Raaw v1.2,” May 2022.
- [26] J. N. Sørensen and W. Z. Shen, “Numerical Modeling of Wind Turbine Wakes,” *Journal of Fluids Engineering*, vol. 124, pp. 393–399, June 2002.
- [27] M. Brazell, S. Ananthan, G. Vijayakumar, L. Cheung, M. Sprague, E. E. C. P. Team, H. F. M. P. Team, *et al.*, “Amr-wind: adaptive mesh-refinement for atmospheric-boundary-layer wind energy simulations,” in *APS Division of Fluid Dynamics Meeting Abstracts*, pp. T29–007, 2021.
- [28] L. Cheung, M. J. Brazell, A. Hsieh, S. Ananthan, G. Vijayakumar, and N. deVelder, “Computation and comparison of the stable northeastern us marine boundary layer,” in *AIAA Scitech 2021 Forum*, p. 0454, 2021.
- [29] D. Allaerts and J. Meyers, “Large eddy simulation of a large wind-turbine array in a conventionally neutral atmospheric boundary layer,” *Physics of Fluids*, vol. 27, p. 065108, June 2015.
- [30] P. K. Taylor and M. J. Yelland, “The Dependence of Sea Surface Roughness on the Height and Steepness of the Waves,” *Journal of Physical Oceanography*, vol. 31, pp. 572–590, Feb. 2001.
- [31] H. Wurps, G. Steinfeld, and S. Heinz, “Grid-Resolution Requirements for Large-Eddy Simulations of the Atmospheric Boundary Layer,” *Boundary-Layer Meteorology*, vol. 175, pp. 179–201, May 2020.
- [32] S. Zilitinkevich, I. Esau, and A. Baklanov, “Further comments on the equilibrium height of neutral and stable planetary boundary layers,” *Quarterly Journal of the Royal Meteorological Society*, vol. 133, pp. 265–271, Jan. 2007.
- [33] Delft High Performance Computing Centre (DHPC), “DelftBlue Supercomputer (Phase 1),” <https://www.tudelft.nl/dhpc/ark:/44463/DelftBluePhase1>, 2022.
- [34] S. Skogestad and I. Postlethwaite, *Multivariable feedback control: analysis and design*. John Wiley & sons, 2005.
- [35] IEC 61400-3: 2019, “Wind energy generation system—part 1,” standard, International Electrotechnical Commission, Geneva, CH, 2019.



Aemilius A. W. van Vondelen was born in Zeist, the Netherlands, in 1997. He received his B.Sc. in Mechanical Engineering and M.Sc. in Systems and Control both from Delft University of Technology, the Netherlands, in 2017 and 2021 respectively. Currently, he is pursuing his Ph.D. at this same institute. His main focus is the development of innovative pitch control solutions for wind turbines and wind farms that balance loads and power gains, where he collaborates closely with industry.



Atindriyo K. Pamososuryo was born in Medan, Indonesia, in 1991. He received his M.Sc. degree from the Delft Center for Systems and Control, Delft University of Technology, the Netherlands, in 2018, where he is pursuing his Ph.D. His research interests include but are not limited to, dynamical system modeling, state estimation, linear parameter varying systems, and model predictive control. In particular, his main focus is on the applications in the wind energy field for advancements in load reduction and power production capabilities at the wind turbine

level, in which he also collaborated with Vestas Wind Systems A/S. In 2023, he received the O. Howard Schuck Award from the American Automatic Control Council for his contribution to the applied control engineering field.



Sachin T. Navalkar was born in Mumbai, India, in 1986. He received his M.Sc. and Ph.D. degrees in sustainable energy and in control engineering from the Delft University of Technology, the Netherlands in 2009 and 2016, respectively. His Ph.D. thesis was entitled Iterative Data-Driven Control for Flexible Wind Turbine Rotors. He is currently Advisory Engineer at Siemens Gamesa Renewable Energy, the Netherlands. His main responsibility is the technology area of load assessment, optimisation, and design solutions for wind turbine support structures.



Jan-Willem van Wingerden (Senior Member, IEEE) was born in Ridderkerk, The Netherlands, in 1980. He received the B.S. and Ph.D. (cum laude) degrees in mechanical engineering and in control engineering from the Delft Center for Systems and Control, Delft University of Technology, Delft, The Netherlands, in 2004 and 2008, respectively. His Ph.D. thesis was entitled Smart Dynamic Rotor Control for Large Offshore Wind Turbines. He is currently a full Professor with the Delft University of Technology. His current research is mainly centered

around the development of data driven controllers for wind turbines and wind farms.